T.&A.M. Report No. 457

SURFACE MOTION EXCITED BY ACOUSTIC EMISSION FROM A BURIED CRACK

by

John G. Harris, Assistant Professor
Associate Member ASME
John Pott, Graduate Student

Department of Theoretical and Applied Mechanics
University of Illinois at Urbana-Champaign
Urbana, Illinois 61801

May 1983

Abstract

The surface motions excited by acoustic emissions produced by fracture processes at the edge of a buried, penny-shaped crack are investigated. Firstly, wavefront approximations to the emissions generated by the sudden growth of a tensile crack in an unbounded elastic solid are reviewed. Then these approximations are Fourier transformed to give the high-frequency portion of their spectra. Secondly, time- and frequency-domain approximations to the surface motions excited by this growing crack, when it is buried in a half-space, are calculated. These results are then scrutinized to elucidate what parts of the signals measured at the surface carry information about the crack's size, its orientation and the fracture processes near the crack-tip.

Introduction

One important source of acoustic emissions, at least in metals, is a tensile crack that suddenly starts to grow. By monitoring these emissions it may be possible to study the fracture processes near the edges of such cracks [1][1] and to assess the severity of these defects in important engineering structures such as pressure vessels [2]. In an attempt to relate the fracture processes to the form of the acoustic emissions, Rose [3] and Achenbach and Harris [4] carried out asymptotic analyses of the waves radiated from models, derived from fracture mechanics, of sudden tensile fractures in unbounded (homogeneous, isotropic, linearly-elastic) media. When the cracks are embedded in an engineering structure, the form of the emissions is also greatly influenced by interaction with the structure's boundaries. To study this Hsu and Hardy [5] measured the response of a plate at a point opposite that at which an excitation, such as the breaking of a glass capillary, was applied and extracted the source time behavior from the overall response by using a transfer function for the plate. Pao [6] has also calculated the response of a plate to various nuclei of strain, which can be used to model sources of acoustic emission. To investigate the combined influence of propagation path and fracture processes, Rose [7], using the body-force equivalents to an elementary tensile and shear crack, calculated the reflection of compressional and shear emissions at a traction-free surface near the epicenter. The purpose of this paper is also to investigate the combined effects of the propagation path and fracture processes. To do so we shall place the model of the growing tensile crack used in [4] in an elastic half-space and calculate the interaction of the acoustic emissions with the

---

[1]Numbers in brackets designate References at the end of the paper.

free surface both near (near field) and far (far field) from the epicenter.

We start by reexamining the asymptotic analysis of acoustic emission begun in [4]. We then use these results to calculate the surface motion excited by the acoustic emissions from a buried, penny-shaped, tensile crack. The crack is assumed to have its plane sufficiently close to the vertical that it can grow toward the surface. We shall be concerned, in the main, with that portion of the measured acoustic emission that arrives first and is strongest. In the near-field we shall calculate the surface motion excited by the incident compressional emission from the point on the crack-edge closest to the surface. We shall also calculate that excited by the incident shear emission, though this signal arrives later. In the far-field the strongest signal is the Rayleigh wave which, though it does not arrive first, constitutes an easily recognized coda. Thus we shall calculate the surface motion in the far-field near the arrival time of the Rayleigh wave that is excited by the point on the crack-edge closest to the surface. This later calculation is done using the same method as that used by Harris, Achenbach and Norris [8] to calculate the Rayleigh waves excited by the starting and stopping phases of a faulting event. Throughout this paper we consider both the time- and frequency-domain results.

Acoustic Emissions from a Growing Tensile Crack

Figure 1 shows a two-dimensional, semi-infinite, tensile crack that is imagined, at $t = 0$, to suddenly start to propagate in its own plane with a constant crack-tip speed c_F. Following reference [4], where this crack-propagation model is discussed at greater length, for small times, and hence for small distances ahead of the original crack-tip, the displacement at the surface of the newly cracked material takes the functional form $F(t - s_F x)$ where

$$F(t) = H(t)\ U\ t^{\nu/2} \tag{1}$$

and $s_F = 1/c_F$. The parameter $\nu = 1$ for brittle fracture, otherwise $\nu > 1$; U is a constant. Achenbach and Harris [4] calculated wavefront approximations to the acoustic emissions from this crack-model. We have repeated their calculations getting the same results, but we have given a different interpretation to the form of the shear emissions in the headwave region of the crack. The results of both these investigations are summarized as follows: The compressional emission $u_r(r,\theta,t)$ near its arrival time $s_L r$, and the shear emission $u_\theta(r,\theta,t)$ near its arrival time $s_T r$ are given by

$$u_r(r,\theta,t) = r^{-1/2}\ E_L(s_F,\theta)e_L(t - s_L r) \tag{2}$$

$$u_\theta(r,\theta,t) = r^{-1/2}[E_{T1}(s_F,\theta)e_T(t - s_T r) + E_{T2}(s_F,\theta)f_T(t,s_T r)] \tag{3}$$

where

$$E_\alpha(s_F,\theta) = S(s_F)\ \Theta_\alpha(\theta),\ \alpha = L,T \tag{4}$$

$$E_{T1}(s_F,\theta) = \mathrm{Re}[E_T(s_F,\theta)];\ E_{T2}(s_F,\theta) = \mathrm{Im}[E_T(s_F,\theta)] \tag{5}$$

$$e_\alpha(t - s_\alpha r) = \frac{1}{\pi}\frac{s_\alpha}{s_R}\frac{1}{(2s_\alpha)^{1/2}}\int_{s_\alpha r}^{t} F(t-\tau)(\tau - s_\alpha r)^{-1/2}d\tau,\ \alpha = L,T \tag{6}$$

$$f_T(t,s_T r) = \frac{1}{\pi}\frac{s_T}{s_R}\frac{1}{(2s_T)^{1/2}}\int_{t_{hw}}^{m} F(t-\tau)(s_T r - \tau)^{-1/2}d\tau\ . \tag{7}$$

The functions $S(s_F)$, $\Theta_L(\theta)$ and $\Theta_T(\theta)$ are given by eqns. (34), (35) and (39) of reference [4], respectively. The constant $s_L = 1/c_L$, $s_T = 1/c_T$ and $s_R = 1/c_R$ where c_L, c_T and c_R are the compressional, shear and Rayleigh wavespeeds. The term $m = \min(t, s_T r)$. Note that the definition of the emission coefficient $E_T(s_F, \theta)$ differs slightly from that given by eqn. (38) of [4].

Equations (2) and (3) represent the compressional and shear cylindrical waves shown in Fig. 1. Also present in the region $\theta_{hw} < |\theta| < \pi$ where

$$\theta_{hw} = \cos^{-1}(-s_L/s_T) \tag{8}$$

is a headwave whose arrival time is t_{hw}. This wave is discussed in [4] where it is given by eqns. (41), (45) and (46). In the headwave region, eqn. (3) differs from the corresponding expression, eqn. (37), in reference [4]. The second term is new; it is non-zero only for $\theta > \theta_{hw}$. Previously only the first term was included in the wavefront approximation in this region. Note that the first term is zero for $t < s_T r$ while the second is not. Thus the new term comes from that portion of the shear wave just ahead of the wavefront at $t = s_T r$. As a result of the square-root singularity at $t = s_T r$, the two-sided cylindrical shear wave makes a more important contribution to the shear emission in the headwave region than does the headwave so that we have not included this latter wave in the summary above. Near $|\theta| = \theta_{hw}$ eqn. (3) is not an accurate description of the wavefield because of the confluence of the headwave and cylindrical-shear wavefronts. A uniform approximation in this region is given by eqns. (37), (47) and (48) of [4].

To extend our results from two dimensions to three we shall make the assumption that, at $t = 0$, all points on the crack-edge start to grow normal to the original crack-edge. Note, however, that this does not imply that c_F is the same at each point on the crack-edge. For this case reference [9] shows that the two-dimensional results can be extended to three-dimensional ones by multiplying the former by $(1 + r/\bar{\rho})^{-1/2}$. This is a first-order correction for the curvature of the crack-edge. The term $\bar{\rho}$ is given by

$$\bar{\rho} = \rho/\cos\theta \tag{9}$$

where ρ is the radius of curvature of the crack-edge. When considering a finite crack there is an additional complication to be noted. The sudden extension of the crack also excites surface waves on the crack-faces which are subsequently diffracted by the crack-edge producing emissions as strong as those first emitted. These emissions can be calculated using the techniques described by Achenbach, Gautesen and McMaken [10]. However, because we are interested in first arrivals we have chosen not to include them here. All these considerations also apply to the frequency-domain results of the next section.

Spectra of the Acoustic Emissions

Wavefront approximations in the time domain correspond to high-frequency results in the frequency domain [11]. Therefore, when calculating the spectra of the transient acoustic emissions given in the previous section, the Fourier transforms can be approximated for large ω , where ω is the angular frequency. The transform pair used here is

$$f(\omega) = \int_{-\infty}^{\infty} e^{i\omega t} f(t)dt \; ; \quad f(t) = \frac{\text{Re}}{\pi} \int_{0}^{\infty} e^{-i\omega t} f(\omega)d\omega \; . \tag{10a,b}$$

An explanation of the particular form of the inverse transform given above can be found in reference [12]. The asymptotic approximation to the Fourier transform of the compressional-wave displacement $u_r(r,\theta,\omega)$ is

$$u_r(r,\theta,\omega) = (s_L/s_R)(2\pi s_L r)^{-1/2} E_L(s_F,\theta)F(\omega)(-i\omega)^{-1/2} e^{i\omega s_L r} \quad (11)$$

where $F(\omega)$ is the Fourier transform of $F(t)$. The asymptotic approximation to the Fourier transform of the shear-wave displacement $u_\theta(r,\theta,\omega)$ is

$$u_\theta(r,\theta,\omega)=(s_T/s_R)(2\pi s_T r)^{-1/2}[E_{T1}(s_F,\theta)(-i\omega)^{-1/2} - E_{T2}(s_F,\theta)b(\omega)]F(\omega)e^{i\omega s_T r} \quad (12)$$

where

$$b(\omega) = \frac{1}{\pi^{1/2}} \int_0^c t^{-1/2} e^{-i\omega t} dt \ . \quad (13)$$

The functions $E_{T1}(s_F,\theta)$ and $E_{T2}(s_F,\theta)$ are given by eqns. (5a,b); the latter function is nonzero only for $|\theta| > \theta_{hw}$. The term $c = (s_T r - t_{hw})$. The function $b(\omega)$ may be approximated as

$$b(\omega) = (i\omega)^{-1/2} - e^{-i\omega c}(\pi c)^{-1/2}(i\omega)^{-1}\{1 + O[(\omega c)^{-1}]\} \ . \quad (14)$$

Retaining only the dominant term in eqn. (14), eqn. (12) becomes

$$u_\theta(r,\theta,\omega) = (s_T/s_R)(2\pi s_T r)^{-1/2} E_T(s_F,\theta)F(\omega)(-i\omega)^{-1/2} e^{i\omega s_T r} \ . \quad (15)$$

Equation (1) expresses $F(t)$ for small t; therefore, $F(\omega)$ for large ω is given by

$$F(\omega) = U\,\Gamma(\nu/2 + 1)(-i\omega)^{-(\nu+2)/2} \ . \quad (16)$$

By using eqn. (10b) to invert eqn. (11) or eqn. (15) we can recover the time-domain wavefront approximations to the compressional and shear emissions given previously except for $|\theta| > \theta_{hw}$, where $E_T(s_F,\theta)$ is complex. This exception arises because, by approximating $b(\omega)$ by only the first term of eqn. (14), we have, in essence, let $t_{hw} \to -\infty$. Thus inverting eqn. (15) in the headwave region leads to eqn. (7) for $f_T(t,s_T r)$ with t_{hw} replaced by $(-\infty)$. But $F(t)$ is known only for small values of its argument, and not in the domain $(0, \infty)$. Therefore we are lead to an integral that has lost its meaning.

Model of a Buried Acoustic Emission Source

In the remaining sections of this paper we shall consider the surface motion excited by the acoustic emissions from a growing tensile crack. The overall geometry is shown in Fig. 2. At $t = 0$ the crack is penny-shaped with radius a. At that instant the crack suddenly begins to grow outwards, normal to the initial crack-edge, with a crack-tip speed that varies along the edge of the crack. The plane of the crack makes an angle ϕ with the normal to the surface. Because we are interested in cracks that grow toward the surface $|\phi|$ is imagined to be small, though technically it need only be less than $\pi/2$. The crack is described by a toroidal coordinate system (r,θ,ψ). The angle ψ defines a point on the crack-edge and, in each plane ψ = constant, (r,θ) form a polar coordinate system whose origin lies at that point. The inset to Fig. 2 shows this for the plane $\psi = 0$. The plane $\psi = 0$ is, moreover, a plane of reflection symmetry. The point B lies in it and is a depth d below the surface. A second coordinate systems (x,y,z) is located with its origin at the intersection of the crack-plane, the symmetry plane and the surface of the half-space. The two coordinate systems are related as follows:

$$x = -d\tan\phi + (a + r\cos\theta)\cos\psi\sin\phi + r\sin\theta\cos\phi - a\sin\phi \qquad (17)$$

$$y = d - (a + r\cos\theta)\cos\psi\cos\phi + r\sin\theta\sin\phi + a\cos\phi \qquad (18)$$

$$z = (a + r\cos\theta)\sin\psi \; . \qquad (19)$$

Note that these coordinate systems are consistent with that used in the previous sections. Though in some cases it is possible to calculate the surface motion out of the plane of symmetry (this point is discussed in appendix B of reference [8]), this is in general difficult so that we eschew it here and confine ourselves to calculations in the symmetry plane. Therefore, the first arrivals will come from point B, where the crack is growing outward at a speed c_F.

Near-Field Surface Motion

The near-field surface motion will be dominated by reflection at the traction-free surface. Because we are interested only in high-frequency or wavefront approximations, the reflected waves may be calculated either by using ray theory [13] or by the integral-representation approach of the next section. These reflected waves are then added to the incident ones to give the net surface motion. The details are omitted.

The net particle displacement at the surface caused by the incident compressional emission is given by

$$\underset{\sim}{u}^{L}(R,\theta) = -\,[R_x^L(\theta)\underset{\sim}{i} + R_y^L(\theta)\underset{\sim}{j}](1 + R\cos\theta/a)^{-1/2}u_r(R,\theta) \qquad (20)$$

where

$$R_x^L(\theta) = \frac{2\kappa\sin[2(\theta + \phi)]\sin\delta}{\kappa^2\cos^2(2\delta) - \sin(2\delta)\sin[2(\theta + \phi)]} \qquad (21)$$

$$R_y^L(\theta) = \frac{2\kappa^2 \cos(2\delta)\ \cos(\theta + \phi)}{\kappa^2 \cos^2(2\delta) - \sin(2\delta)\ \sin[2(\theta + \phi)]} \tag{22}$$

$$R = d/\cos(\theta + \phi) \tag{23}$$

and $u_r(R,\theta) = u_r(R,\theta,t)$ (eqn. (2)) or $u_r(R,\theta,\omega)$ (eqn. (11)) for the time-domain or frequency-domain results, respectively. The angle δ is given by

$$s_T \cos\delta = - s_L \sin(\theta + \phi) \tag{24}$$

and $\kappa = s_T/s_L$. The net particle displacement at the surface caused by the incident shear emission is given by

$$\underset{\sim}{u}^T(R,\theta) = - [R_x^T(\theta)\underset{\sim}{i} + R_y^T(\theta)\underset{\sim}{j}](1 + R\cos\theta/a)^{-1/2} u_\theta(R,\theta) \tag{25}$$

where

$$R_x^T(\theta) = \frac{2\kappa^2 \cos(\theta + \phi)\ \cos[2(\theta + \phi)]}{\kappa^2 \cos^2[2(\theta + \phi)] - \sin(2\gamma)\ \sin[2(\theta + \phi)]} \tag{26}$$

$$R_y^T(\theta) = \frac{-\ 2\sin(2\gamma)\ \cos(\theta + \phi)}{\kappa^2 \cos^2[2(\theta + \phi)] - \sin(2\gamma)\ \sin[2(\theta + \phi)]} \tag{27}$$

and $u_\theta(R,\theta) = u_\theta(R,\theta,t)$ (eqn. (3)) or $u_\theta(R,\theta,\omega)$ (eqn. (15)) for the time-domain or frequency-domain results, respectively. The distance R is given by eqn. (23) and the angle γ by

$$s_L \cos\gamma = - s_T \sin(\theta + \phi)\ . \tag{28}$$

Note that for values of $(\theta + \phi)$ such that

$$s_T\left|\sin\ (\theta + \phi)\right| > s_L \qquad (29)$$

γ becomes imaginary and both $R_x^T(\theta)$ and $R_y^T(\theta)$ become complex. This is caused by the incident shear wave exciting a critically reflected compressional wave at the surface. Therefore, for values of $(\theta + \phi)$ satisfying eqn. (29) the above expression, eqn. (25), is valid in the frequency domain but not in the time domain.

The phenomena indicated by eqn. (29) has been examined within the context of the present analytical framework by Harris and Achenbach [14]. Here it is enough to note that eqn. (25) in the frequency domain has the same analytical structure in the region defined by eqn. (29) as does the shear emission, eqn. (15), in the headwave region of the crack. Further, near points such that eqn. (29) becomes an equality, uniform approximations are needed to understand the surface motion completely, just as in the case of the crack a uniform approximation is needed near θ_{hw} .

To illustrate these results consider the special case $\phi = 0$. The normalized horizontal ($i = x$) and vertical ($i = y$) amplitudes of the net surface motion are

$$A_i^\alpha = \left|(s_\alpha/s_L)^{1/2}\ R_i^\alpha(\theta)[(R/d)(1 + R\cos\theta/a)]^{-1/2}\ E_\alpha(s_F,\ \theta)\right| \qquad (30)$$

where $\alpha = L$ when the incident emission is compressional and $\alpha = T$ when it is shear. In Fig. 3 we have plotted the A_i^L against $\overline{x} = x/d$ for $d/a = 2$, Poisson's ratio = 0.25 and $s_T/s_F = 0.5$. Also plotted are the corresponding horizontal and vertical amplitudes of the incident compressional emission. As expected reflection amplifies the incident disturbance. Moreover, the figure shows that for $\bar{x} = 20$ the surface motion due to reflection has decayed to less than 20% of its maximum. Thus, for our model of an acoustic-emission event, we can estimate that the near field ends near that point (also see conclusion 2). In Fig. 4 we have plotted the A_i^T against $\bar{x}$ for the same parameters, as well as the corresponding components of the incident shear emission. The large spike in Fig. 4a and the zero in Fig. 4b indicate the point at which $s_T \sin\theta = s_L$. As indicated above the present calculation is not accureate near this point; however, it is possible to conclude that the surface motion varies rapidly near this point. Comparison of Figs. 3 and 4 (note that these two figures have quite different scales) shows that, except in a localized region directly above the crack-tip, the compressional emission is the more important. In the time domain this motion will also be the first excited.

More generally, note that in the frequency domain the surface displacement, whether it be that given by eqn. (20) or eqn. (25), is directly proportional to $F(\omega)(-i\omega)^{-1/2}\exp(i\omega s_\alpha R)$. The particle displacement at the surface would thus decay at high frequencies as $\omega^{-(\nu+3)/2}$. A measurement of this decay, by assigning a value to ν , would give some indication of the fracture processes at the crack-tip.

Far-Field Surface Motion

The far-field surface motion will be dominated by the presence of a Rayleigh wave. We shall begin by considering this wave in the frequency domain and then use eqn. (10b) to extend our results to the time domain. The method of calculation employed here is identical to that used in reference [8] to calculate the Rayleigh wave excited by a faulting event. There it was shown that the Fourier components of the displacement of the first-arriving Rayleigh wave $\underset{\sim}{u}^R(\underset{\sim}{x},\omega)$ could be expressed as

$$u_k^R(\underset{\sim}{x},\omega) = \int_{S_i} [u_{i;k}^{GR}(\underset{\sim}{x}',\underset{\sim}{x},\omega)\tau_{ij}^I(\underset{\sim}{x}',\omega) - u_i^I(\underset{\sim}{x}',\omega)\tau_{ij;k}^{GR}(\underset{\sim}{x}',\underset{\sim}{x},\omega)]n_j dS(\underset{\sim}{x}') \quad (31)$$

where S_i is a surface enclosing the crack-edge and $\underset{\sim}{n}$ is a unit normal pointing inward. The terms $u_{i;k}^{GR}$ and $\tau_{ij;k}^{GR}$ are the Rayleigh-wave components of the Green's displacement and stress tensors for the elastic half-space [15]. The terms $u_i^I(\underset{\sim}{x},\omega)$ and $\tau_{ij}^I(\underset{\sim}{x},\omega)$ consist of the sum of the compressional and shear waves emitted by the crack as it starts to grow. We are interested in high-frequency results; therefore, we can approximate $u_i^I(\underset{\sim}{x},\omega)$ by an appropriate sum of the displacements given by eqns. (11) and (15). Further we need only the high-frequency approximations to $u_{i;k}^{GR}$ and $\tau_{ij;k}^{GR}$. The surface integral eqn. (31) now consists of a compressional-wave part and a shear-wave part. The former is evaluated by selecting S_i to be the wavefront of the compressional part of $u_i^I(\underset{\sim}{x},\omega)$ and then approximating the integral asymptotically; the latter is similarly evaluated using the shear-wave wavefront.

As a result of the calculations described above, the frequency-domain expressions for the Rayleigh-wave displacement in the plane of symmetry are

$$\begin{aligned} \underset{\sim}{u}^R(x,y,o,\omega) = 4(1/\kappa_R)[g_L E_L(s_F,\theta)\exp(-i\omega s_L \underset{\sim}{\bar{p}}^L \cdot \underset{\sim}{x}_B) - \\ - g_T \cot(2\theta_T)\, E_T(s_F,\theta)\exp(-i\omega s_T \underset{\sim}{\bar{p}}^T \cdot \underset{\sim}{x}_B)] \times \\ \times \underset{\sim}{U}(\underset{\sim}{x},\omega)\, D_o^{-1}\, F(\omega)e^{i\pi/2} \end{aligned} \quad (32)$$

where θ takes the specific values $\theta = \pi/2 - \phi - \theta_L$ in $E_L(s_F, \theta)$ and $\theta = \pi/2 - \phi - \theta_T$ in $E_T(s_F,\theta)$. The angles θ_α are given by

$$\theta_\alpha = i \cosh^{-1}(s_R/s_\alpha) \tag{33}$$

The major terms $\underset{\sim}{U}(\underset{\sim}{x},\omega)$, g_α, $E_\alpha\ (s_F,\theta)$ and $F(\omega)$ are given by

$$\underset{\sim}{U}(\underset{\sim}{x},\omega)=2(1/\kappa_R\kappa^2)[\underset{\sim}{d}^L\exp(i\omega s_L\underset{\sim}{p}^L\cdot\underset{\sim}{x})\ (1/\kappa)\cot(2\theta_T)\underset{\sim}{d}^T\exp(i\omega s_T\underset{\sim}{p}^T\cdot\underset{\sim}{x})] \tag{34}$$

$$g_\alpha = [1 + \frac{d}{a}\,(\frac{x}{d} + \tan\phi)\ \frac{\sin(\phi + \theta_\alpha)}{\cos\theta_\alpha}\ ]^{-1/2} \tag{35}$$

eqn. (4) and eqn. (16), respectively. The various ancillary expressions are as follows:

$$\underset{\sim}{p}^\alpha = \cos\theta_\alpha\ \underset{\sim}{i} + \sin\theta_\alpha \underset{\sim}{j} \tag{36}$$

$$\underset{\sim}{d}^L = \underset{\sim}{p}^L\ ;\quad \underset{\sim}{d}^T = \underset{\sim}{k} \times \underset{\sim}{p}^T \tag{37}$$

$$\underset{\sim}{x} = x\,\underset{\sim}{i} + y\underset{\sim}{j}\ ;\quad \underset{\sim}{x}_B = -\,d\tan\phi\ \underset{\sim}{i} + d\underset{\sim}{j} \tag{38}$$

$$D_o = [\kappa_R\kappa^2(\kappa_R^2 - \kappa^2)^{1/2}]^{-1}\ \frac{d}{dt}[4t^2(t^2 - \kappa^2)^{1/2}(t^2 - 1)^{1/2} - (\kappa^2 - 2t^2)^2] \tag{39}$$

where $\kappa = s_T/s_L$, $\kappa_R = s_R/s_L$ and, in eqn. (39), $t = \kappa_R$. For Poisson's ratio $= 0.25$, $D_o = 6.2$. The subscript or superscript α in each of the above terms is either L or T, the L indicating the compressional term and the T the shear term. The overbars in eqn. (32) denote the complex conjugate.

Time-domain results are obtained from the above expressions by using eqn. (10b). Near the Rayleigh-wave arrival time the particle velocities are given by

$$\dot{\underset{\sim}{u}}^R(x,y,o,t) = (2\kappa_R U/\kappa^2 D_o)(s_R d)^{(\nu-2)/2}[v_1(x,y,t)\underset{\sim}{i} + v_2(x,y,t)\underset{\sim}{j}] \tag{40}$$

where

$$v_i(x,y,t) = \frac{4}{\pi}\Gamma\left(\frac{\nu+2}{2}\right)\Gamma\left(\frac{2-\nu}{2}\right) \sum_{\alpha,\beta=L,T} v_i^{\alpha\beta}(x, y, t) \tag{41}$$

$$v_i^{\alpha\beta}(x,y,t) = \frac{A_i^{\alpha\beta}\cos\{[(2-\nu)/2]\tan^{-1}(B^{\alpha\beta}) - \theta_i^{\alpha\beta} - (\nu\pi/4)\}}{(C^{\alpha\beta})^{(2-\nu)/2}[1 + (B^{\alpha\beta})^2]^{(2-\nu)/4}} \tag{42}$$

$$A_i^{\alpha\beta}\exp(i\theta_i^{\alpha\beta}) = d_i^{\alpha}\ S^{\alpha\beta}\ g_\beta\ E_\beta(s_F,\ \pi/2 - \phi - \theta_\beta)e^{i\pi/2} \tag{43}$$

$$B^{\alpha\beta} = [(t/s_R d) - (x/d + \tan\phi)]/C^{\alpha\beta} \tag{44}$$

$$C^{\alpha\beta} = [1 - (s_\alpha/s_R)^2]^{1/2}(y/d) + [1 - (s_\beta/s_R)^2]^{1/2}\ . \tag{45}$$

In eqns. (41)-(45), $i = 1,2$ and $\alpha,\beta = L,T$. The terms $S^{\alpha\beta}$ are given by

$$S^{LL} = 1\ ;\quad S^{TL} = (s_T/s_L)\cot(2\theta_T) \tag{46a,b}$$

$$S^{LT} = -(s_L/s_T)\cot(2\theta_T);\quad S^{TT} = -\cot^2(2\theta_T). \tag{46c,d}$$

The parameter ν must satisfy the inequalities $1 \leqslant \nu < 2$, where $\nu \geqslant 1$ for physical reasons (eqn. (1)), while $\nu < 2$ in order that the particular transform inversion used to calculate eqns. (40)-(45) remain valid. This range of ν includes the important case of brittle fracture ($\nu = 1$). We chose to calculate the Rayleigh-wave particle velocities rather than the displacements because, for the special case of brittle fracture, the waveform functions of the incident emissions are step functions, making a comparison with the Rayleigh waveform clearer.

For the results above we have adopted the following sign convention. The angle ϕ can take positive or negative values, but $(x + d \tan\phi)$ is always assumed to be positive. This, however, means that θ is positive in a downward sense for ϕ positive, but is positive in an upward sense for ϕ negative. The horizontal distance from the crack-tip, in the plane of symmetry, is $(x + d \tan\phi)$ so that when ϕ is varied this distance changes even though x is fixed.

The arrival time, which follows from $B^{\alpha\beta} = 0$ (eqns. (42) and (44)), suggests that the Rayleigh wave is emitted from a point directly above the crack-tip. However, no Rayleigh wave can exist at the surface unless the incident waves properly couple to the surface [16]. As a consequence a position at the surface where a Rayleigh wave is observed must satisfy one of the inequalities

$$[(x/d) + \tan\phi] > [(s_R/s_\alpha)^2 - 1]^{-1/2} \qquad (47)$$

where $\alpha = L$ or T. Taking the more stringent of the two, and setting Poisson's ratio = 0.25, gives $[(x/d) + \tan\phi] > 2.3$. However, as we discussed earlier, we are interested in regions where x/d is of the order of 20 for $\phi = 0$, so that these inequalities are satisfied.

In the frequency domain the orientation of the crack influences the Rayleigh wave through the emission coefficients $E_\alpha(s_F, \pi/2 - \phi - \theta_\alpha)$ and through the geometrical spreading factors g_α. Figure 5 plots the magnitudes of the emission coefficients versus ϕ, for Poisson's ratio = 0.25 and

$s_T/s_F = 0.5$. Note that θ_α is complex so that these coefficients are being evaluated at complex angles. This figure should be compared with Figs. 3 and 4 of reference [4] where the emission coefficients $E_L(s_F,\theta)$ and $E_{T1}(s_F,\theta)$ are plotted for real θ. Of particular interest are the peaks for negative ϕ. In the case of the compressional emission coefficient such a peak does not appear for real angles near $(3\pi/4)$. In the case of the shear emission coefficient, the negative values of ϕ mean that it is being evaluated in the headwave region. Thus even through the crack is orientated so that any emissions from the headwave region of point B would not strike the surface, knowledge of the emission coefficient in that region is essential if the Rayleigh waves are to be calculated. Note also, that, whereas for real angles the shear emission coefficient goes to zero at $|\theta| = \theta_{hw}$, for complex angles its behavior is much more regular near θ_{hw}.

The magnitudes of the spreading factors have maxima for certain values of the triad $(\bar{x},\bar{d},\phi)$, where $\bar{x} = x/d$ and $\bar{d} = d/a$. However, for values of $\bar{d} = O(1)$ and $|\phi| = O(\pi/4)$ or less, and Poisson's ratio = 0.25, the maxima occur for values of $\bar{x}$ that do not satisfy the inequalities expressed by eqn. (47). Thus for the values of $\bar{x}$ considered here the spreading factors fall off approximately as $(\bar{x})^{-1/2}$, the geometrical decay for a Rayleigh wave excited by a point source. This situation should be compared with that of reference [8], where, for $\bar{d} = 0.5$ and $\phi = -30°$, the spreading factors do have maxima for values of $\bar{x}$ that also satisfy eqn. (47).

Comparison of eqn. (32) with eqns. (20) and (25) shows the interesting fact that, whereas the reflected waves carry the spectral term $F(\omega)(-i\omega)^{-1/2}\exp(i\omega s_\alpha R)$, the Rayleigh-wave displacement, at the surface, carries $F(\omega)$ multiplied by terms containing $\exp\{-\omega[(s_\alpha/s_R)^2 - 1]^{1/2}d\}$ times $\exp[i\omega s_R(x + d\tan\phi)]$. Thus the high-frequency spectrum of the Rayleigh wave will fall off exponentially rather than algebraically, with the fall-off determined by ωd .

The influence of the depth d can also be seen in the time domain. The depth dependence of the Rayleigh-wave particle velocity manifests itself through the normalizing term $(s_R d)^{(\nu-2)/2}$ in eqn. (40) and through the term $(C^{\alpha\beta})^{(2-\nu)/2}$ in eqn. (42). Note that for $\nu = 1$ (brittle fracture) the decay with depth is greatest. Figure 6 shows the normalized components of the particle velocities $v_i(x, y, t)$ $(i = 1, 2)$ evaluated at $y = 0$ plotted against $\tau = \bar{t} - \bar{x}$, where $\bar{t} = t/(s_R d)$. The parameters in this figure are $\phi = 0$, $\bar{x} = 20$, $\nu = 1$, Poisson's ratio = 0.25 and $s_T/s_F = 0.5$; in (a) $\bar{d} = 2$ and in (b) $\bar{d} = 5$. Comparison of (a) with (b) shows that the signal strength decreases as the size of the crack decreases and its depth increases.

More generally, note that in the time domain the geometry of the problem and the time-dependence of the problem are mixed together by the presence of the angle $\theta_i^{\alpha\beta}$ in the cosine term in eqn. (42). Equation (43) shows that $\theta_i^{\alpha\beta}$ comes from the geometrical factors g_α and $E_\alpha(s_F, \pi/2 - \phi - \theta_\alpha)$ evaluated at the complex angle θ_α. This should be contrasted with the incident emissions, eqns. (2) and (3), for which the geometry and the time-dependence can be separated near their wavefronts. This becomes particularly striking for $\nu = 1$ as mentioned earlier.

Conclusions

The results of this paper lead to the following conclusions:

1. In the headwave region of the crack, the dominate contribution to the shear-wave emission comes from the region near $t = s_T r$ for both $t > s_T r$ and $t < s_T r$. As a consequence we were led to redefine the shear-wave emission coefficient $E_T(s_F, \theta)$ using eqns. (4) and (5a,b). In the frequency domain this leads to the simple result eqn. (15). Figure 5 and the

accompanying discussion show how essential this analysis is to calculating the Rayleigh wave. In essence the Rayleigh-wave calculation demanded a knowledge of $E_L(s_F, \theta)$ and $E_T(s_F, \theta)$ for all θ, including complex θ.

2. Our study of the near-field surface motion has shown that, in addition to being the first to arrive, the surface motion caused by the incident compressional emission dominates that caused by the incident shear emission except in a localized region directly above the crack-tip. In the far field the Rayleigh wave, though it is a later arrival, becomes the dominant disturbance. A comparison of the amplitude terms in Fig. 3 with the peaks in the Rayleigh wave in Fig. 6 shows that for $\nu = 1$ the ratio of $|\dot{u}_x|$ at $\bar{x} = 20$ to $|\dot{u}_x^R|$ at $\tau = 0$ is 1.

3. A measurement of acoustic emission should in principle, give information about the crack's size, its orientation and the fracture processes near the crack-tip. Certainly size and orientation affect the emission as we have tried to show by our study of the parameters θ, ϕ , $\bar{d}$ in Figs. 3-6. But perhaps the most interesting result is our determination of how the spectral function $F(\omega)$, which is directly determined by the fracture processes at the crack-tip, is modified by the propagation effects in the near and far field.

Acknowledgment

The work reported here was carried out in the course of research sponsored by the Solid Mechanics Program of the Division of Mechanical Engineering and Applied Mechanics, National Science Foundation, NSF Grant MEA 81-04738. Moreover, we wish to thank Richard L. Weaver for his helpful comments.

References

1. Wadley, H. N. G. and Scruby, C. B., "A Study of Deformation and Fracture Processes in a Low-Alloy Steel by Acoustic Emission Transient Analysis," Acta Metallurgica, Vol. 27, 1979, pp. 613-625.

2. Spanner, J. D., "Acoustic Emission, Applications and Trends," Elastic Waves and Non-Destructive Testing of Materials, Pao, Y.-H., ed., AMD Vol. 29, ASME, New York, pp. 71-84.

3. Rose, L. R. F., "The Stress-Wave Radiation from Growing Cracks," International Journal of Fracture, Vol. 17, 1981, pp. 45-60.

4. Achenbach, J. D. and Harris, J. G., "Acoustic Emission From a Brief Crack Propagation Event," ASME Journal of Applied Mechanics, Vol. 46, 1979, pp. 107-112.

5. Hsu, N. N. and Hardy, S. C., "Experiments in Acoustic Emission Waveform Analysis for Characterization of A. E. Sources, Sensors and Structures," Elastic Waves and Non-Destructive Testing of Materials, Pao, Y.-H., ed., AMD Vol. 29, ASME, New York, pp. 85-106.

6. Pao, Y.-H., "Theory of Acoustic Emission," Elastic Waves and Non-Destructive Testing of Materials, Pao, Y.-H., ed., AMD Vol. 29, ASME, New York, pp. 107-128.

7. Rose, L. R. F., "On the Acoustic Emission Due to the Fracture of Brittle Inclusions," Journal of Nondestructive Evaluation, Vol. 1, 1980, pp. 149-155.

8. Harris, J. G., Achenbach, J. D. and Norris, A. N., "Rayleigh Waves Excited by the Discontinuous Advance of a Rupture Front," Journal of Geophysical Research, Vol. 88, 1983, pp. 2223-2239.

9. Ahluwalia, D. S., Keller, J. B. and Jarvis, R., "Elastic Waves Produced by Surface Displacements," SIAM Journal of Applied Mathematics, Vol. 26, 1974, pp. 108-119.

10. Achenbach, J. D., Gautesen, A. K. and McMaken, H., Ray Methods for Waves in Elastic Solids, Pitman, Boston, 1982, pp. 133-138.

11. Lighthill, M. J., Fourier Analysis and Generalized Functions, Cambridge University Press, Cambridge, 1958, pp. 46-58.

12. Cerveny, V. and Ravindra, R., Theory of Seismic Head Waves, University of Toronto Press, Toronto, 1971, pp. 93-96.

13. Ibid. [10], pp. 89-108.

14. Harris, J. G. and Achenbach, J. D., "Near-Field Surface Motions Excited by Radiation From a Slip Zone of Arbitrary Shape," Journal of Geophysical Research, Vol. 86, 1981, pp. 9352-9356.

15. Ibid. [10], pp. 63-73.

16. Ewing, W. M., Jardetzky, W. S. and Press, F., Elastic Waves in Layered Media, McGraw-Hill, New York, 1957, pp.63-66.

"Surface Motion Excited by Acoustic Emission from a Buried Crack" by John G. Harris and John Pott

Figure Captions

Fig. 1 Acoustic emission from a tensile crack that suddenly starts to grow with speed c_F.

Fig. 2 A penny-shaped tensile crack growing in a plane which makes an angle ϕ with the vertical. At the instant shown, point B, which lies in the symmetry plane $\psi = 0$, is a distance d below the surface and is moving toward the origin 0 .

Fig. 3 The amplitudes of (a) the horizontal A_x^L and (b) the vertical A_y^L surface motion are plotted against $\bar{x}$. The angle $\phi = 0$, $d/a = 2$, Poisson's ratio = 0.25 and $s_T/s_F = 0.5$.

Fig. 4 The amplitudes of (a) the horizontal A_x^T and (b) the vertical A_y^T surface motion are plotted against $\bar{x}$. The angle $\phi = 0$, $d/a = 2$, Poisson's ratio = 0.25 and $s_T/s_F = 0.5$.

Fig. 5 The magnitudes of the emission coefficients $|E_\alpha(s_F, \theta)|$ evaluated at $\theta = \pi/2 - \phi - \theta_\alpha$, $\alpha = L, T$, are plotted against ϕ. Poisson's ratio = 0.25 and $s_T/s_F = 0.5$.

Fig. 6 The normalized components of the Rayleigh-wave particle velocity v_i, $i = 1, 2$, at the surface are plotted against $\tau = \bar{t} - \bar{x}$. In (a) $\bar{d} = 2$ and in (b) $\bar{d} = 5$. In both $\phi = 0$, $\bar{x} = 20$, $\nu = 1$, Poisson's ratio = 0.25 and $s_T/s_F = 0.5$.

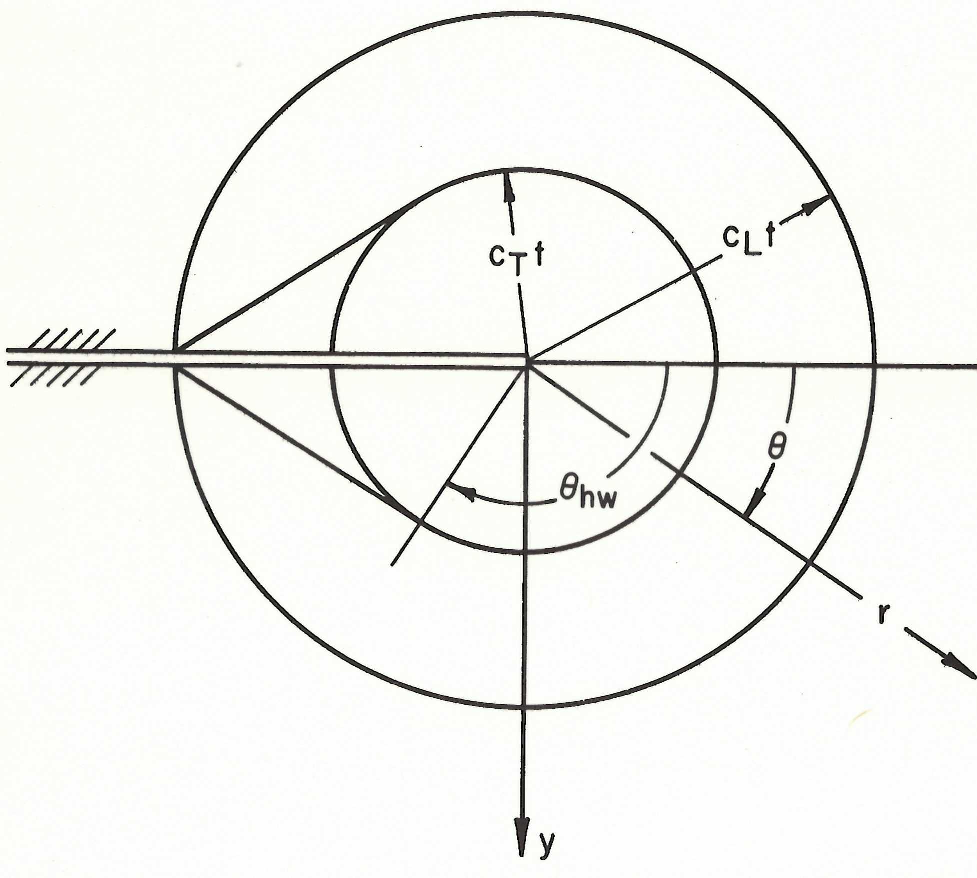

$c_T t$
$c_L t$
x
θ
θ_{hw}
r
y

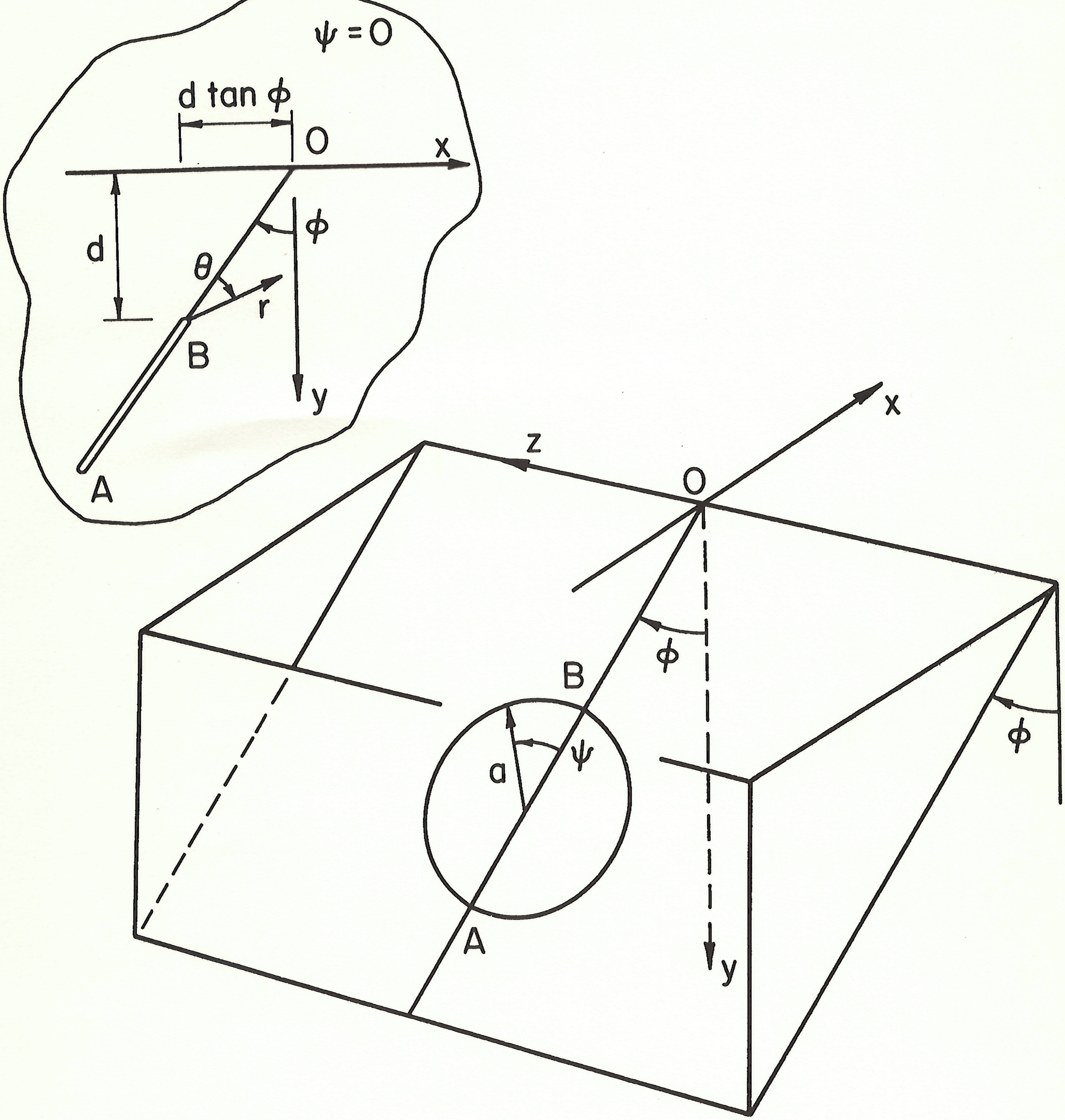
ψ = 0
d tan φ
O
x
d
φ
θ
r
B
y
A
z
O
x
φ
B
a
ψ
φ
A
y

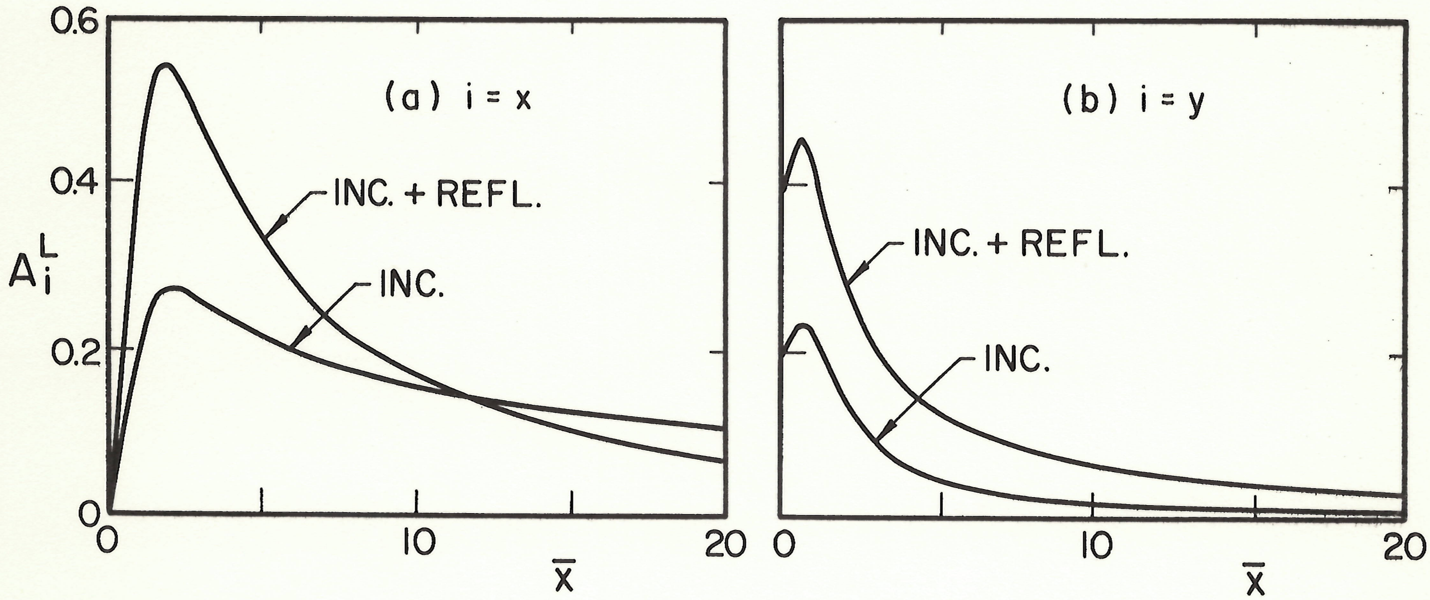
0.6
0.4
0.2
0
A_i^L
(a) i = x
INC. + REFL.
INC.
0
10
20
$\bar{x}$
(b) i = y
INC. + REFL.
INC.
0
10
20
$\bar{x}$

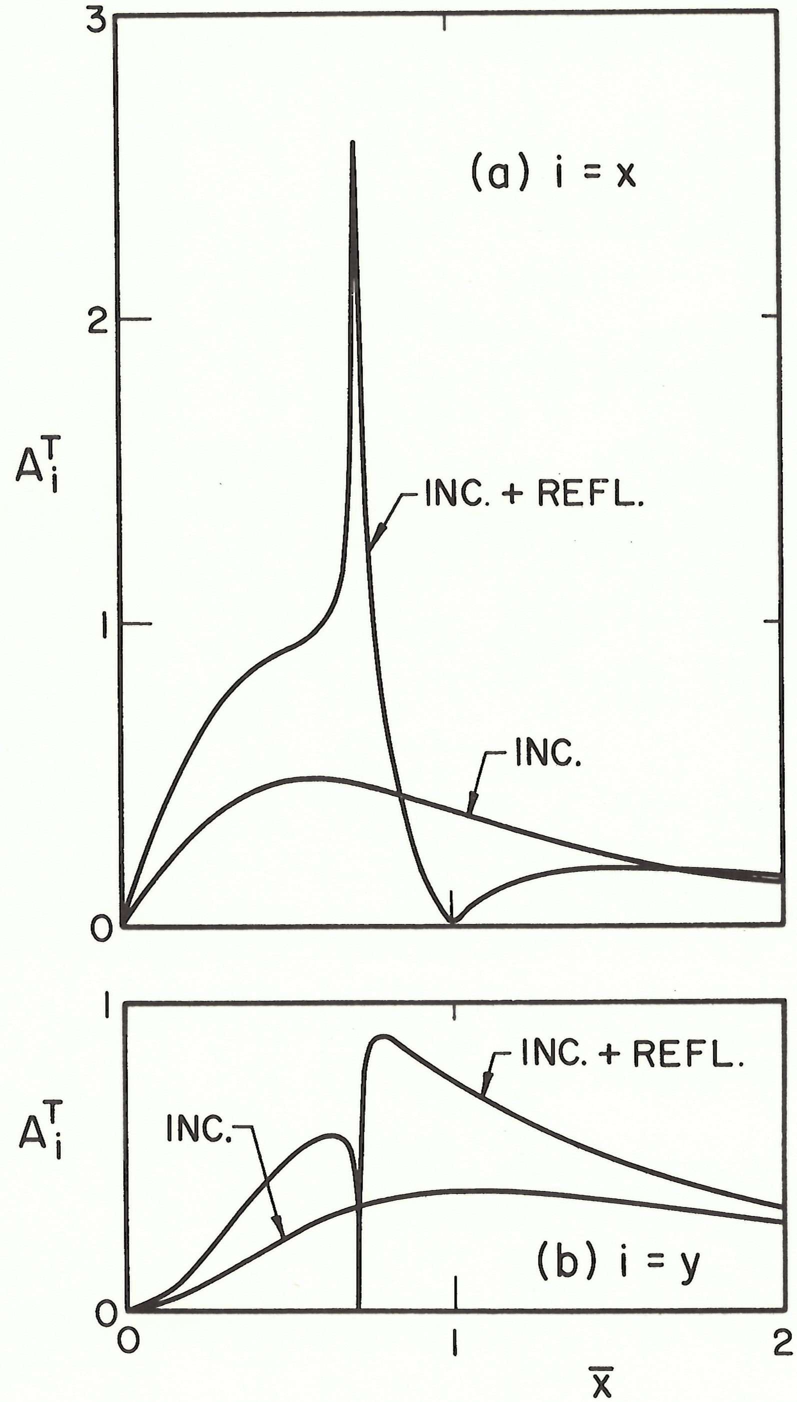
3
2
1
0
A_i^T
(a) i = x
INC. + REFL.
INC.
1
0
A_i^T
INC. + REFL.
INC.
(b) i = y
0
1
2
$\bar{x}$

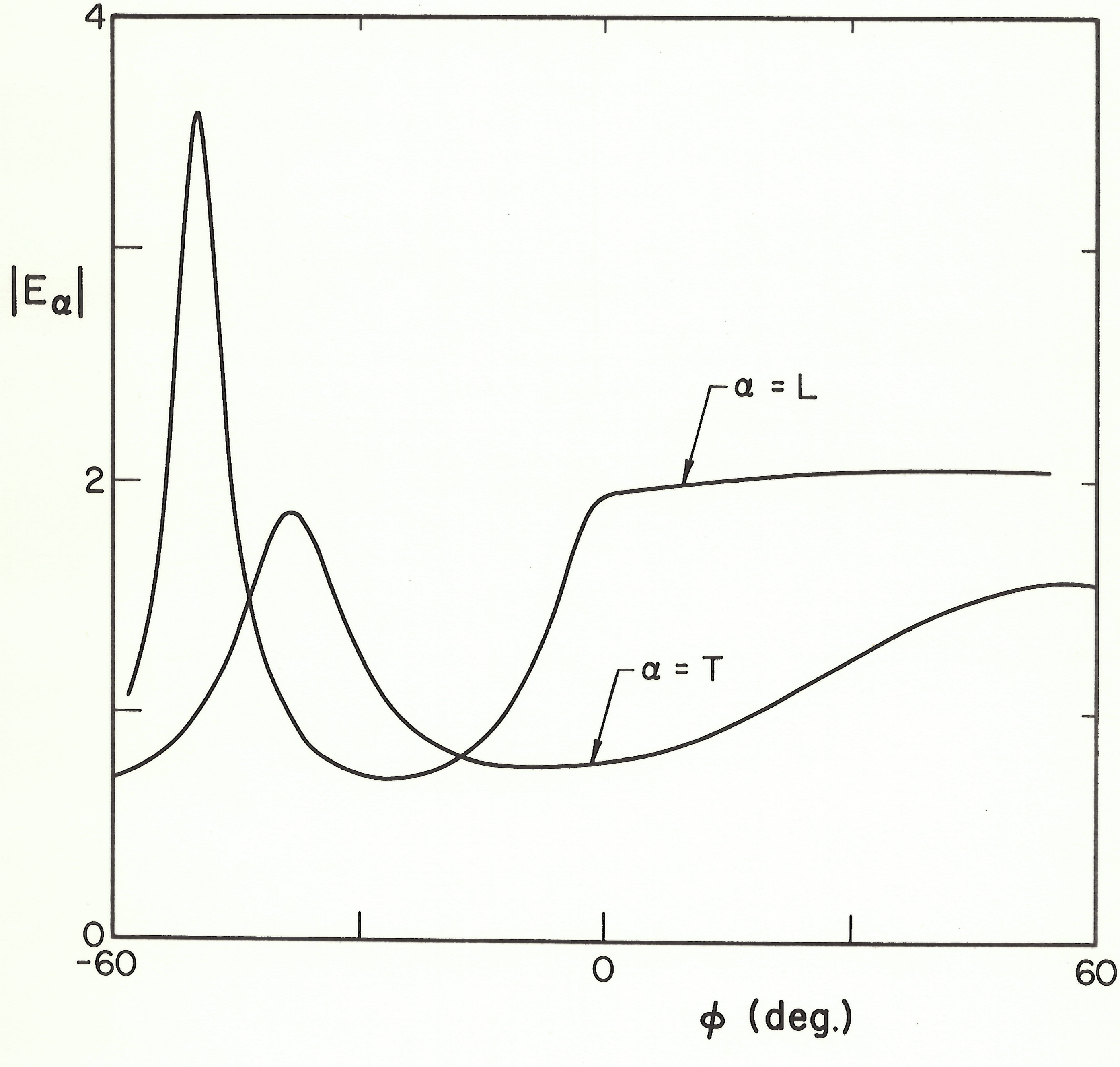
4
2
0
|Eα|
α = L
α = T
-60
0
60
φ (deg.)

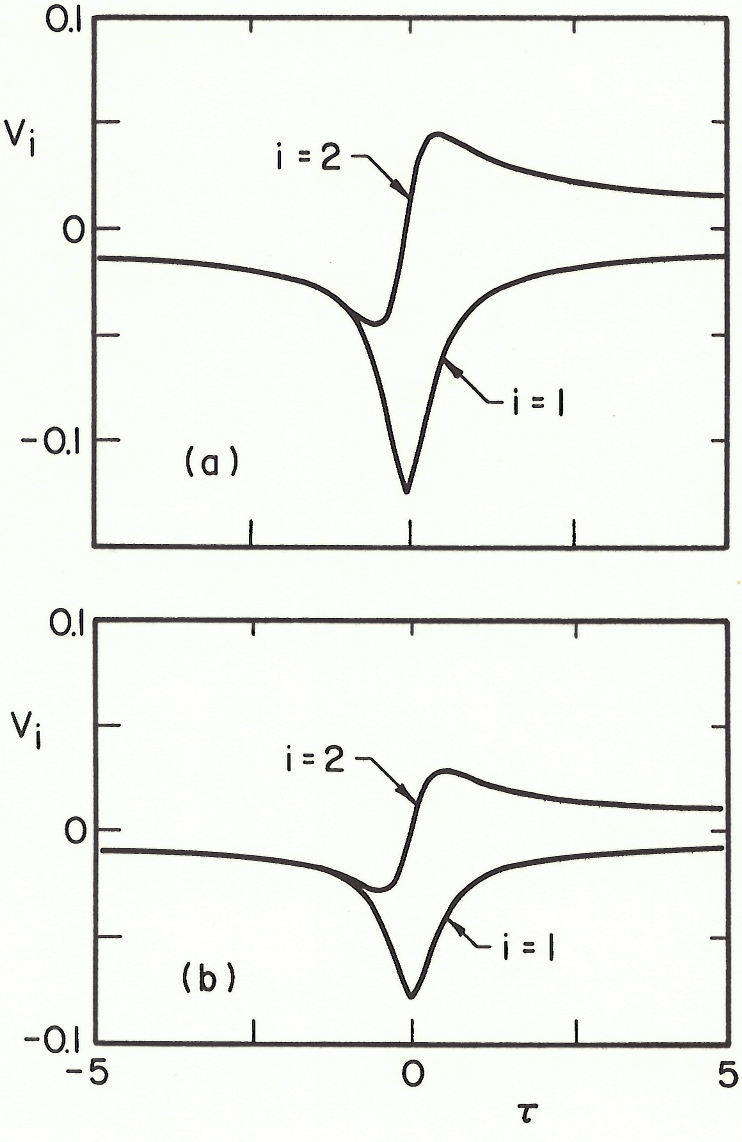
0.1
V_i
i = 2
0
i = 1
-0.1
(a)
0.1
V_i
i = 2
0
i = 1
(b)
-0.1
-5
0
5
τ